Catalysis Today 357 (2020) 664–674

Contents lists available at ScienceDirect

Catalysis Today

journal homepage: www.elsevier.com/locate/cattod

Review

Effects induced by interaction of the $Pt/CeO_x/ZrO_x/\gamma\text{-}Al_2O_3$ ternary mixed oxide $DeNO_x$ catalyst with hydrogen

Stanislava Andonova[a,*], Zehra Aybegüm Ok[b], Emrah Ozensoy[b,c,**], Konstantin Hadjiivanov[a,d]

[a] Institute of General and Inorganic Chemistry, Bulgarian Academy of Sciences, 1113, Sofia, Bulgaria
[b] Chemistry Department, Bilkent University, 06800, Bilkent, Ankara, Turkey
[c] UNAM-National Nanotechnology Center, Bilkent University, 06800, Ankara, Turkey
[d] Bulgarian Academy of Sciences, Sofia, 1040, Bulgaria

ARTICLE INFO

Keywords:
$DeNO_x$ catalyst
NO_x Reduction
$Pt/CeO_x/ZrO_x/\gamma\text{-}Al_2O_3$
H_2
D_2
D/H exchange

ABSTRACT

Effects of H_2/D_2 adsorption on the surface chemistry of $Pt/CeO_x\text{-}ZrO_x/\gamma\text{-}Al_2O_3$ $DeNO_x$ catalyst were investigated. *In-situ* FTIR spectroscopy and NO_x-TPD techniques were utilized to monitor changes in the surface chemistry of studied materials. Adsorption studies of CO and O_2 revealed that the Pt/Ce-Zr/Al sample, initially reduced with H_2 at 723 K, is characterized by the presence of oxygen vacancies in close vicinity of Ce^{3+} centres and metallic Pt sites. Adsorption of O_2 occurred through the formation of superoxide $(O_2^-)_{ads}$ species and oxidation of Ce^{3+} to Ce^{4+} ions. The ability of the catalyst to activate molecular O_2 originates from its relatively high population of oxygen vacancies located on/near the surface. Interaction of Pt/Ce-Zr/Al system with H_2 or D_2 takes place through heterolytic dissociation at ambient temperature. D_2 adsorption leads to the reduction of Ce^{4+} to Ce^{3+} ions and formation of adsorbed molecular heavy water and gradual D/H exchange with the existing surface hydroxyl groups. Generated D_2O interacts with isolated hydroxyls/deuteroxyls through H-bonding and this provokes the formation of H-bonded O—H/O—D groups. These later species are relatively stable and gradually vanish with increasing temperatures above 523 K, leaving behind only isolated hydroxyls. Surfaces enriched with H-bonded hydroxyls are characterized with an enhanced NO_x storage ability revealing their significant role in low-temperature NO_x adsorption mechanism.

1. Introduction

The need for better fuel economy and the ever-increasing environmental requirements restricting the NO_x emissions in particular from diesel-equipped vehicles have driven the development of different technologies of NO_x reduction in oxygen rich conditions. Over the past several years the most prominent $DeNO_x$ technologies that received considerable attention as economical and effective solutions for catalytic abatement of NO_x pollutants in excess oxygen were the selective catalytic reduction (SCR) of NO_x and NO_x storage/reduction (NSR) [1–4].

In an attempt to improve the catalytic performance, numerous studies focused on the design of different $DeNO_x$ catalytic systems with long-term durability and improved sulfur resistance. Ceria (CeO_2) and/or M/ceria/γ-alumina based materials (M = Pt, Pd, Rh) are commonly used as the key components in the applications geared towards controlling the lean-NO_x emissions from mobile sources [5–9]. These catalysts typically consist of noble metal active sites to facilitate the NO_x reduction process, a ceria-zirconia mixed oxide promoter to enhance the oxygen storage capacity (OSC) and a high-surface-area support material to achieve good metal/promoter dispersion. Ceria is a promising component used in a vast number of $DeNO_x$ catalysts with varying structures and compositions, due to its unique oxidation-reduction properties [9,10]. The main catalytic functionality of CeO_2 originates from Ce cations in its structure which can switch between different oxidation states (*e.g.* Ce^{4+} and Ce^{3+}) and the capability of the crystal lattice to create/heal oxygen vacancies in a reversible manner [10,11]. Hence, CeO_2 can store or transport oxygen in or out of the ceria matrix under oxidizing or reducing conditions in redox reactions, respectively. It is known [12] that ceria can act as a buffer to supply oxygen during the oxygen deficient (*i.e.* rich) periods of the engine operation and conversely uptake oxygen when there is an excess of O_2 in the exhaust stream (*i.e.* under lean conditions). CeO_2 can also function as an effective promoter [4,13–15] leading to a significant

* Corresponding author at: Institute of General and Inorganic Chemistry, Bulgarian Academy of Sciences, 1113, Sofia, Bulgaria
** Corresponding author at: Chemistry Department, Bilkent University, 06800, Bilkent, Ankara, Turkey.
E-mail addresses: s.andonova@svr.igic.bas.bg (S. Andonova), ozensoy@fen.bilkent.edu.tr (E. Ozensoy).

https://doi.org/10.1016/j.cattod.2019.02.056
Received 13 December 2018; Received in revised form 12 February 2019; Accepted 22 February 2019
Available online 23 February 2019
0920-5861/

Table 1
Composition of the synthesized samples, specific surface area (S_{BET}) and calculated parameters *via* XRD (Pt average particle size, noble metal dispersion).

Samples	CeO_2 *wt. %*	ZrO_2 *wt. %*	$\gamma-Al_2O_3$ *wt. %*	Pt *wt. %*	S_{BET} m^2 g^{-1}	Pt average particle size, *nm**	MD_{Pt}**
γ-Al_2O_3	–	–	100	–	200	–	–
Ce-Zr/Al	10	10	80	–	174	–	–
Pt/Ce-Zr/Al	10	10	80	1	142	29	0.38

*Average Pt particle size values were determined *via* XRD.
*To evaluate the platinum dispersion (MD_{Pt}), the relationship between mean Pt particle size and the dispersion was used.

improvement in NO_x reduction, sulfur regeneration and thermal resistance properties of NSR catalysts. Ceria-based systems were studied [16–18] for their low-temperature NO_x storage capabilities due to the anionic vacancies that can be formed in the fluorite crystal structure which have been found to facilitate the NO_x adsorption. Ceria promotion is also known [13] to have a strong influence on the dispersion of precious metals on metal oxide support materials.

To tune the OSC and thermal stability of the (Pt, Pd, Rh)/ceria-alumina based materials, a variety of synthetic protocols [19,20] can be utilized, where mixed oxide systems can be designed by the incorporation of foreign cations (with different sizes and oxidation states) into the cubic fluorite lattice of CeO_2. Numerous studies [21–25] dealt with the performance of the $Pt/CeO_2–ZrO_2/\gamma$-Al_2O_3 system as a $DeNO_x$ catalyst under conditions simulating the NO_x reduction process. This catalytic architecture was found [26] to have a great potential for the NO_x elimination process because of the pronounced redox properties of ceria and its strong interaction with the precious transition metal. Incorporation of zirconium in the ceria component is known to improve the catalytic performance [25,26] by enhancing the resistance of the material to sintering, while expediting the reducibility of ceria, leading to a greater population of oxygen vacancies which are responsible for the activity of the catalyst towards oxygen-containing molecules. Moreover, $Ce_{1-x}Zr_xO_2$ mixed oxides are known to have a high NO_x adsorption capacity due to the various basic centers on their surfaces [12]. The presence of ZrO_2 can also inhibit the undesirable interaction of CeO_2 with Al_2O_3, preventing the deactivation of the Ce(IV)/Ce(III) redox couple due to formation of $CeAlO_3$ [11].

Despite the numerous investigations on $DeNO_x$ processes carried out with Pt/CeO_2-ZrO_2/Al_2O_3 mixed ternary oxide system [26–28], effects induced by the interaction of the catalyst with hydrogen used as a reducing agent in the NO_x reduction process are still not sufficiently well known. Efforts in our previous work [29] were focused on the surface chemistry and elucidation of the nature of the adsorbed NO_x species on the Pt/CeO_2-ZrO_2/Al_2O_3 catalyst. Parallel studies were also carried out with benchmark samples such as: CeO_2/Al_2O_3, ZrO_2/Al_2O_3, CeO_2-ZrO_2/Al_2O_3 and Pt supported versions of these materials. Despite the high thermal stability of the NO_x adsorbed species on the ceria and zirconia adsorption sites, we have shown [29] that the NO_x reduction in the presence of H_2 is much more facile over the Pt/CeO_2-ZrO_2/Al_2O_3 catalyst. It was concluded [29] that the main difference in the functionality could be related to the ability of the catalyst to activate hydrogen at relatively lower temperatures.

Along these lines, as a continuation of our previous report [29], current study focuses on the effects induced by the interaction of the Pt/CeO_x-ZrO_x/γ-Al_2O_3 system with H_2. In this study, based on *in-situ* Fourier-transform infrared spectroscopy (FTIR) investigations, we report our results on the effect of H_2 or D_2 on the activated Pt/CeO_x-ZrO_x/γ-Al_2O_3 catalyst and also provide data on the NO_x reactivity of the investigated material pre-exchanged with D_2. Further information regarding the thermal stability of the NO_x adsorbed species was acquired from the NO_x-temperature programmed desorption (TPD) analysis. In order to obtain a comprehensive picture, *in-situ* FTIR adsorption studies were also carried out by using CO and O_2.

2. Experimental

2.1. Sample preparation

Commercial γ-alumina (γ-Al_2O_3, 200 m^2/g, SASOL Puralox SBa-200) was used as the primary support material in the synthesis of the ternary mixed oxide $Pt/CeO_x/ZrO_x/\gamma$-Al_2O_3 system. Ceria and zirconia were deposited on γ-alumina by conventional incipient wetness impregnation. For this purpose, appropriate amounts of aqueous solutions of $Ce(NO_3)_3{\cdot}6H_2O$ (Sigma Aldrich, 99.99%) and/or $ZrO(NO_3)_2{\cdot}xH_2O$, *Sigma Aldrich* 99.99%) were used in order to achieve 10 wt. % of CeO_2 + 10 wt. % of ZrO_2 in the final product. The precursor solutions were mixed with γ-Al_2O_3 and the slurry was continuously stirred. This is followed by evaporation at 350 K until the water from the suspension was completely removed. The resulting solid was then dried and calcined at 873 K for 2 h. The mixed oxide support material was further functionalized with the addition of platinum. For this purpose, a Pt precursor solution ($Pt(NH_3)_2(NO_2)_2(aq)$; 3.4 wt % in dilute ammonium hydroxide, Sigma Aldrich) was prepared and then the support material was slowly added to the solution under constant stirring at room temperature (RT). Next, the slurry was continuously stirred, and the solvent was evaporated at 350 K. Finally, the product was ground into a fine powder form and calcined at 973 K for 2.5 h. The nominal noble metal loading is 1 wt. % Pt. For convenience, some basic characteristics of the synthesized samples are summarized in Table 1.

2.2. Characterization techniques

The BET (Brunauer–Emmett–Teller) specific surface areas (S_{BET}, $m^2\,g^{-1}$) of the calcined samples were determined by low–temperature isothermal adsorption–desorption of N_2 using a Micromeritics Tristar 3000 apparatus. The measurements were performed on previously degassed samples (573 K for 2 h) using nitrogen adsorption data within the relative equilibrium pressure interval of 0.03–0.3 P/P^0 according to the standard 5-point BET procedure. The X-ray diffraction (XRD) patterns were obtained with a Rigaku diffractometer, equipped with a Miniflex goniometer and an X-ray source with CuKα radiation, at λ = 1.5418 A, 30 kV, and 15 mA. Diffraction patterns of the samples were recorded in 2θ range between 10 and 80° with a step size of 0.01° s^{-1}. The patterns were assigned using Joint Committee on Powder Diffraction Standards (JCPDS) cards supplied by the International Centre for Diffraction Database (ICDD). To evaluate the surface metal dispersion (MD_{Pt}) of the Pt catalysts, the relationship between [30] mean Pt particle size (d_{Pt}) and the dispersion was used. Thus, the MD was estimated according to Eq. (1), as follows:

$$MD_{Pt} = 6\frac{(\vartheta_m/a_m)}{d_{pt}} \quad (1)$$

where the volume v_m occupied by an atom Pt in the bulk of metal is given by the equation: $v_m = M/\rho N_A$ where M is the atomic mass of Pt, ρ the mass density and N_A Avogadro's number. In the case of platinum (M = 195.08 g mol^{-1}; ρ = 21.45 g cm^{-3}), $v_m = 15.10A^3$. The surface area a_m occupied by an atom Pt on a polycrystalline surface is 8.07 A^2.

NO_x–temperature programmed desorption (TPD) experiments were performed by using a quadrupole mass spectrometer (QMS, SRS

RGA200) directly connected to custom-designed TPD-*in-situ* FTIR spectroscopic system. In the TPD experiments, the sample (*ca.* 20 mg of finely ground powder) was pressed onto a high transmittance lithographically etched fine-tungsten grid which was mounted on a copper sample holder assembly attached to a ceramic vacuum feedthrough. A K-type thermocouple was spot-welded to the surface of a thin tantalum plate attached on the W-grid to monitor the sample temperature. The sample temperature was controlled within 298–1100 K *via* a computer-controlled DC resistive heating system using the voltage feedback from the thermocouple. To minimize the effect of NO oxidation/adsorption/disproportionation on Pt which could affect the total amount of NO_x adsorbed species, the NO_x storage ability tests over the samples were thus performed by using of NO_2 as the adsorbent. Prior to each experiment, to obtain a surface that is free of adsorbed NO_x and other adsorbates (such as carbonates), the sample was heated to 1023 K in vacuum with a constant rate of 12 K min^{-1}. After cooling to 323 K, NO_x storage experiments were performed. Before the NO_x TPD experiments, the samples were exposed to 5 Torr of NO_2 for 10 min until equilibrium was reached. After this exposure/saturation step, the sample was outgassed to $\sim 10^{-7}$ Torr to remove weakly adsorbed (physisorbed) NO_x species and subsequently a TPD analysis was carried out with a heating rate of 12 K min^{-1}. N_2, NO, O_2, N_2O and NO_2 contents of the desorbing gas mixture were monitored *on-line* by following the desorption signals corresponding to the mass to charge ratio (*m/z*) values of 28, 30, 32, 44, and 46, respectively. The NO_x adsorption ability of the catalysts was estimated by calculating the total integrated areas under NO_x related desorption features in the TPD profiles after considering fragmentation patterns of all the major NO_x desorption species (*i.e.* NO_2, NO, N_2, N_2O). Thus, to normalize the data, the intensity of the signals for each gas was corrected by a factor using the standard mass spectroscopic fragmentation databases of the National Institute of Standards and Technology (NIST) [31] (See Supplementary materials).

FTIR spectroscopic measurements were carried out in transmission mode using *Nicolet Avatar 6700* FTIR spectrometer, equipped with a Hg–Cd–Te (MCT) detector. The experiments were performed in a batch-type IR cell equipped with optically polished CaF_2 windows allowing data acquisition at low (100 K) and ambient temperatures. The cell was directly connected to a vacuum-adsorption apparatus with a residual pressure lower than 1×10^{-6} Torr.

For the FTIR experiments, self-supporting pellets (*ca.*10 mg cm^{-2}) were used. They were prepared by pressing the sample powders at a pressure of $\sim$ 5 Ton cm^{-2}, applied for 1–2 min. Then, the pellets were placed inside the IR cell using a custom-made movable sample holder that allows insertion of the sample in the middle of the heated zone of the IR cell. Thus, the spectra were registered *in-situ* after each thermal treatment of the sample at different temperatures and atmospheres. Each FTIR spectrum was acquired within the 4000–800 cm^{-1} spectral region by accumulating 64 scans at a spectral resolution of 2 cm^{-1}. The background and gas phase corrections were performed using the Omnic software.

The samples were analysed in activated and reduced forms. The activation was performed by heating the self-supporting pellets at 673 K in air for 1 h with a subsequent evacuation at the same temperature to a residual pressure $\sim 2 \times 10^{-6}$ Torr. The reduced forms were obtained by heating the pellets at 723 K in 22.5 Torr H_2 for 1 h followed by evacuation at 673 K to a residual pressure around 2×10^{-6} Torr.

FTIR investigations were performed before and after adsorption of different gases on the catalyst surfaces either at RT or at low temperature (100 K). Carbon monoxide/nitrogen monoxide (CO, NO, > 99.9% pure) were supplied by *Air Liquide, France*), while oxygen, hydrogen and deuterium (O_2, H_2 and D_2, > 99.9% pure) were obtained from *Messer*. Prior to the experiments, all gases were purified by passing through a liquid nitrogen trap, while NO was additionally purified by fractional distillation.

3. Results and discussion

3.1. Preliminary structural characterization: surface area and noble metal dispersion

The BET specific surface area (S_{BET}) of Pt–free Ce-Zr/Al sample was found to be $\sim$174 m^2 g^{-1} (see Table 1). This is about 13% lower as compared to the pure $\gamma-Al_2O_3$ (200 m^2/g) which was used as the primary support material in the synthesis. Deposition of Pt leads to an additional decrease in S_{BET} by 18%. These observations can be associated with partial blocking of the $\gamma-Al_2O_3$ pore structure by oxide- and Pt-containing crystallites.

Crystal structural analysis of the Pt/Ce-Zr/Al sample *via* X-ray diffraction (XRD) was reported in one of our recent study [29], where it was observed that ceria existed as a crystalline CeO_2 phase with a fluorite structure, while zirconia revealed a disordered/amorphous form, and/or a highly-dispersed oxide phase with a small particulate size. Average particle size and dispersion of Pt on the CeO_2-ZrO_2/Al_2O_3 system were investigated *via* XRD and transmission electron microscopy (TEM). Major diffraction signal of Pt (111) at $2\theta = 39.7^\circ$ was utilized [32] to calculate the average Pt particle size using the *Scherrer equation*. Thus, the parameters calculated from the XRD analysis revealed that the Pt average particle size on Pt/Ce-Zr/Al catalyst was about 29 nm (Table 1). It was also evident that the dispersion of the metal platinum on the Pt/Ce-Zr/Al sample was relatively low (MD_{Pt} ~ 0.38). TEM analysis [29] clearly indicated the presence of both aggregated Pt crystallites with an average size of $\sim$30 nm as well as some smaller Pt particles which were more homogeneously distributed on the surface. The redox behaviour of both Ce-Zr/Al and Pt/Ce-Zr/Al systems was also studied by temperature programmed reduction with H_2 [29] and the results revealed that ceria in the Pt/Ce-Zr/Al catalyst was mostly in the form of a highly dispersed defective phase due to its interaction with the noble metal sites. As a result, reduction of this defective ceria phase occurred at lower temperatures (~471 K) and in a facile manner.

3.2. In-situ FTIR spectroscopic adsorption studies

3.2.1. Background FTIR spectra

The FTIR spectra of the activated and reduced forms of the Pt/Ce-Zr/Al sample in the ν(O—H) stretching region are presented in Fig. 1A. For comparison, the spectrum of pure γ-alumina used as a reference is shown in Fig. 1B.

The spectra in the hydroxyl stretching region of the Pt/Ce-Zr/Al sample seem to be hardly sensitive to Ce and/or Zr incorporation as well as the pretreatment steps (activation/reduction). Indeed, the spectra of the activated and reduced forms (Fig. 1A, spectra *a* and *b*, respectively) are very similar to the spectrum of alumina (Fig. 1B), which is the main component in the ternary mixed oxide material. The spectrum of alumina contains three well-resolved bands with maxima at 3770, 3729 and 3680 cm^{-1}. These bands can be assigned based on former literature reports [33,34]. The most prominent band at 3729 cm^{-1} is assigned to hydroxyls bridging two Al^{3+} sites having an octahedral coordination (Type-IIa hydroxyl) while the band at 3680 cm^{-1} is attributed to OH groups bound to three octahedrally coordinated Al^{3+} sites (Type-III hydroxyl). The band at 3770 cm^{-1} is associated with the terminal OH groups (Type-Ia hydroxyl) on the single tetrahedrally coordinated Al^{3+} sites that can exist on two different crystallographic orientations (*i.e.* (111) and (110)) of the γ-Al_2O_3 surface. In addition, a shoulder at $\sim$ 3790 cm^{-1} and a broad band around 3593 cm^{-1} are also visible. The feature at ~ 3790 cm^{-1} is attributed to the presence of hydroxyls bound to a single octahedrally coordinated Al^{3+} sites (type-Ib hydroxyl) while the broad feature at $\sim$3593 cm^{-1} characterizes H-bonded hydroxyls. It should be noticed that the intensity of the band at 3770 cm^{-1} in the spectra of the Pt/Ce-Zr/Al is lower and appears as shoulder, compared to that in the spectrum of γ-Al_2O_3 (Fig. 1B). On the other hand, a new IR feature at

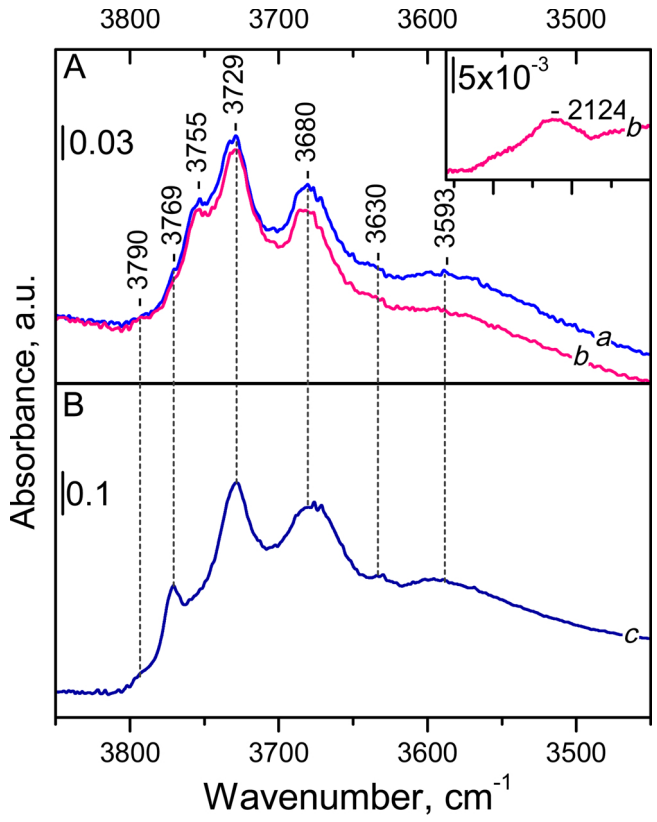

Fig. 1. FTIR background spectra of the activated (a) and reduced (b) Pt/Ce-Zr/Al sample in the ν(O—H) stretching region (Panel A). Panel B shows the background spectrum (c) of pure γ-Al_2O_3 in the ν(O—H) stretching region. The inset of the figure shows the spectra of the reduced (b) Pt/Ce-Zr/Al sample within the spectral region 2260-2000 cm^{-1}.

3755 cm^{-1} becomes visible in the spectra of the Pt-containing system. The same band is also observed in the spectra of Pt/CeO_2/γ-Al_2O_3 and Pt/ZrO_2/γ-Al_2O_3 binary oxide benchmark samples, presented in our former work [29]. Thus, the band 3755 cm^{-1} is not likely due to the incorporation of ceria and zirconia. This feature can be associated with hydroxyl groups of the support (those characterized by the band at 3769 cm^{-1}) and deposited Pt species which may also induce attenuation of the band at 3769 cm^{-1} and the appearance of a new feature at 3755 cm^{-1}.

It is known [35–37] that IR spectroscopy can be a very efficient technique to follow the degree of ceria reduction. Change of the oxidation state of cerium can be detected by the appearance of an IR band with a maximum at *ca.* 2124 cm^{-1} in the spectrum of the reduced Pt/Ce-Zr/Al system (inset of Fig. 1A, spectrum b). This feature is associated with the forbidden $^2F_{5/2} - {}^2F_{7/2}$ electronic transition of Ce^{3+} ions and its presence is indicative of oxygen vacancy formation [34,36,37]. Presence of the feature given in the inset of Fig. 1A clearly indicated the existence of Ce^{3+} ions on the reduced Pt/Ce-Zr/Al system.

3.2.2. CO adsorption at low temperature (100 K)

To obtain detailed information regarding the nature of metallic sites on the Pt/Ce-Zr/Al sample and in attempt to investigate various types of surface acid sites on the catalyst surface, low-temperature CO adsorption was carried out on both activated and reduced forms of the Pt/Ce-Zr/Al sample. In these experiments, CO (2.25 Torr CO equilibrium pressure) was introduced into the IR cell at 100 K. After having reached equilibrium, the spectra were acquired under evacuation at constant temperature (*i.e.* decreasing the CO coverage). Thus, all spectral changes were followed as function of the CO isothermal coverage decrease. Fig. 2 presents the FTIR spectra in the ν(CO) stretching region registered after low-temperature adsorption of CO (2.25 Torr CO equilibrium pressure) on activated (A) and reduced (B) forms of the Pt/Ce-Zr/Al sample (spectrum *a*) and evolution of the spectra under dynamic vacuum at 100 K (spectra *b*–*q*). The insets of the figure show the spectral changes in the ν(OH) stretching region.

Adsorption of CO (2.25 Torr CO equilibrium pressure) on the activated Pt/Ce-Zr/Al has resulted initially to the development of three principal bands in the ν(CO) region with maxima at 2187, 2178 and 2155 cm^{-1} (Fig. 2A, spectrum *a*). The process is accompanied by the appearance of two negative bands located in the ν(OH) stretching region (the inset of Fig. 6A), at 3735 cm^{-1} and 3762 cm^{-1} while a new band at 3617 cm^{-1} was observed to grow. The gradual decrease of the CO coverage upon evacuation (spectra *b*–*q*) leads to an overall blue shift of the bands in the CO stretching region and progressive attenuation of the IR intensities until their full disappearance. As observed, the intensity of the most prominent band at 2155 cm^{-1} decreases more significantly and its disappearance from the spectra enabled identification of the bands at 2180 and 2197 cm^{-1} clearly (see spectra l–q). After prolonged evacuation at 100 K, it can be seen that the initial spectrum is practically restored (see the inset of Fig. 2A).

The most intense band at 2155 cm^{-1} can be attributed to CO polarized by OH groups [34]. This assignment is supported by the observation of negative OH stretching bands at 3762 and 3735 cm^{-1} corresponding to the disappearance of isolated surface hydroxyl functionalities due to CO adsorption and CO interaction with isolated surface OH groups. These OH—CO complexes can easily be destroyed upon evacuation. The bands at 2187 and 2178 cm^{-1} are assigned to CO interacting with the Al^{3+} and Ce^{4+} cations [29,38] through the formation of physisorbed carbonyl species. These series of spectra clearly indicates that, as expected, the carbonyl species on the Lewis acid sites (Ce^{4+} and Al^{3+}) are more stable than that of the OH groups. It should be noticed that the positions of the carbonyl bands are often coverage-dependent due to lateral interaction between the adsorbed CO molecules. The shift of the band from 2187 to 2197 cm^{-1} is not discrete but rather gradual, indicating that the band at 2197 cm^{-1} is also due to the carbonyls on the same adsorption sites assigned to the feature at 2187 cm^{-1}. In the case of the band at 2187 cm^{-1}, again the shift to 2180 cm^{-1} is gradual but is much smaller. This indicates that the respective adsorbed species are isolated and are not interacting strongly.

In our previous study [29], we reported that during the synthesis of the ternary mixed oxide system, deposited ceria was preferentially located at the Lewis acid sites, while deposited zirconia preferentially interacted with the alumina hydroxyls.

The preliminary reduction of the Pt/Ce-Zr/Al sample at 723 K with H_2 (22.5 Torr) resulted in several changes in the spectra of adsorbed CO (Fig. 2B). Adsorption of CO on reduced Pt/Ce-Zr/Al sample (Fig. 2B spectra a) results in the formation of Pt^0-CO species as evident by the appearance of IR features within 2100-2000 cm^{-1} region [39–42]. It is visible that the adsorption led to the development of a broad band at *ca.* 2081 cm^{-1} with a shoulder at ~ 2060 cm^{-1} revealing a minor feature at around 2099 cm^{-1}. The band at 2081 cm^{-1} and its shoulder slightly shifted to higher frequencies upon evacuation and even gained some intensity (Fig. 2B, spectra *b*–*q*). This observation can be explained by reduction of cationic Pt sites to form metallic Pt^0 during the CO desorption. It is well known [39,40] that the ν(CO) frequency is sensitive to the Pt coordination and shifts to lower frequencies when the Pt coordination decreases. Thus, the observed features in this work were assigned to linear carbonyls located on metallic Pt that exists on the surface with different particle sizes. In particular, we assign the band at 2086 cm^{-1} to CO adsorption on terrace sites of the Pt(111) surface of large platinum crystallites [41], while the feature at ~ 2060 cm^{-1} is mainly due to CO adsorbed on the (111) facets of smaller Pt nanoparticles [39]. The small feature at around 2099 cm^{-1} is ascribed to atop CO species on Pt(111) with a high CO surface coverage [42].

In addition, adsorption of CO on the reduced Pt/Ce-Zr/Al system also led to the appearance of two well resolved bands with maxima at

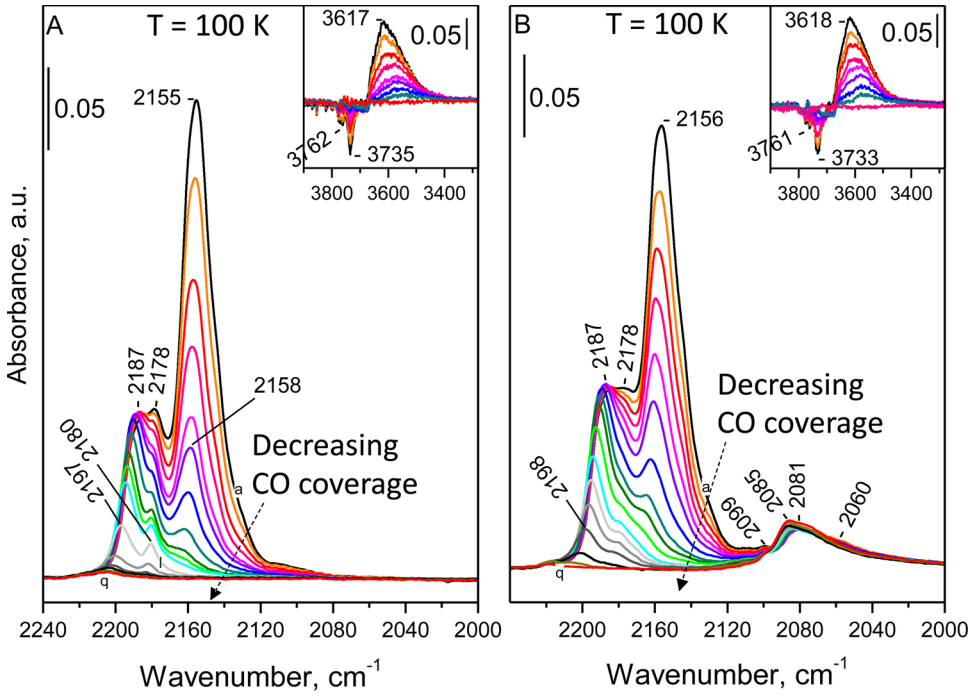

Fig. 2. FTIR spectra in the ν(C—O) stretching region of CO (2.25 Torr equilibrium pressure) adsorbed at 100 K on activated (panel A) and reduced (panel B) Pt/Ce-Zr/Al sample (spectrum *a*) and evolution of the spectra during evacuation at 100 K (*b*–*q*). The insets of the figure show the spectral changes in the ν(O—H) stretching region. The spectra are background and CO gas-phase corrected.

2156 and 2187 cm^{-1} in the CO stretching region and a shoulder at ~ 2178 cm^{-1}. However, comparison of the spectra in Fig. 2A and B reveals that the band at 2187 cm^{-1} with the shoulder at ~ 2178 cm^{-1} (assigned to $Al^{3+}-CO$ and $Ce^{4+}-CO$) appeared with slightly increased intensity in Fig. 2B. This observation may indicate that after the formation of metal particles due to reduction, some of the adsorption sites on the support surface which were formerly bound to Pt species are liberated and become available for further CO adsorption [34,43]. It should also be noted that the shoulder at 2178 cm^{-1} is less pronounced for the reduced sample which is in line with the proposed assignment.

3.2.3. O_2 adsorption at low temperature (100 K)

In order to understand the adsorption and dissociation of O_2 on the Pt/Ce-Zr/Al sample surface and to obtain information on the presence of oxygen-deficient adsorption sites, adsorption of O_2 (g) was carried out.

In these experiments, precisely controlled small doses of O_2 equivalent to ~ 4.8×10^{-3} μmol each were successively introduced onto the pre-reduced Pt/Ce-Zr/Al sample at 100 K until an equilibrium O_2 pressure of 3.75 Torr was reached in the IR cell. Fig. 3 presents the corresponding FTIR spectra in the ν(O—O) stretching region associated with the adsorbed oxygen species formed upon gradual increase of the O_2 pressure (spectra *a*–*h*) and evolution of the spectra upon successive evacuation (spectra *h*–*t*) with a gradual decrease of the oxygen coverage. The inset of Fig. 3 shows the background spectra of the pre-reduced sample before O_2 adsorption (*spectrum bg*) and the spectrum recorded after the first small dose of O_2 (*spectrum a*).

Introduction of the first small doses of O_2 onto the pre-reduced sample initially resulted in a complete re-oxidation of ceria. This can clearly be seen in the inset of Fig. 3 where the feature at 2128 cm^{-1} observed for the reduced sample (background *spectrum bg*) before O_2 adsorption completely vanished from spectrum (*a*) after the first small dose of O_2. Disappearance of this particular feature is an indication that Ce^{3+} sites on ceria are readily oxidized to Ce^{4+} due to the healing of the defects (*i.e.* filling of the oxygen vacancies) on the pre-reduced Pt/Ce-Zr/Al surface.

Step-wise increase in the equilibrium O_2 pressure on the Pt/Ce-Zr/Al sample surface resulted in the development of three weak but well-resolved bands in the ν(O—O) vibration region revealing maxima at 1132, 1142 and 1148 cm^{-1} (Fig. 3, spectra *a*–*h*). The gradual decrease in the O_2 pressure upon evacuation (spectra *h*–*t*) led to an overall red shift of the bands and a monotonic attenuation of the IR intensities. Particularly, the band at 1142 cm^{-1} was observed to be very unstable and quickly disappeared from the spectra in the very early stages of evacuation. Additional O_2 adsorption experiments performed at room temperature and higher O_2 pressures such as 150 Torr (see Fig. S1, "Supplementary materials"), also resulted in the appearance of similar bands tough with much lower intensities and slightly lower frequencies (1129, 1139 and 1144 cm^{-1}). These weak bands were found to be unstable and almost completely disappeared after prolonged evacuation at 298 K.

According to the literature [44–46], the bands located at 1132 cm^{-1} or 1129 cm^{-1} which were observed during O_2 adsorption can be attributed to the characteristic frequency of the (O—O) vibration due to the formation of adsorbed superoxide (O_2^-) species in close proximity of the Ce^{4+} sites. It has also been reported in various previous studies [44–46] that surface superoxide species can be formed as a result of the interaction between molecular oxygen with the oxygen vacancies located in the close vicinity of the Ce^{3+} centres. It is likely that after the adsorption of molecular oxygen on vacancies, a neighbouring Ce^{3+} species can donate an electron to adsorbed molecular oxygen leading to the reduction of oxygen to form superoxide ions and oxidation of Ce^{3+} to Ce^{4+} through reactions (2) and (3).

$$O_2(g) + {}^*(vacancy) \rightarrow O_2(ads) \quad (2)$$

$$Ce^{3+}(surf) + O_2(ads) \rightarrow Ce^{4+}(surf) + O_2^-(ads) \quad (3)$$

It should be noticed that if the oxygen vacations are linked to two Ce^{3+} ions then the adsorbed oxygen could oxidize only one of them. However, the absence of Ce^{3+} ions on the surface after the initial dose of O_2 indicates that it is more likely that each Ce^{4+} ion is surrounded by only one anion radical. This could explain why the adsorbed superoxide (O_2^-) species disappear relatively easily upon evacuation.

It has been reported in the literature [47–49] that incorporation of zirconia to the ceria structure may enhance oxygen activation and superoxide formation which are the key steps in surface oxygen transport, diffusion and oxygen storage. Furthermore, presence of noble metal (*e.g.* Rh, Pt, Pd) sites [47–49] in close contact with ceria may also enable oxygen adsorption, activation and storage by contributing to the

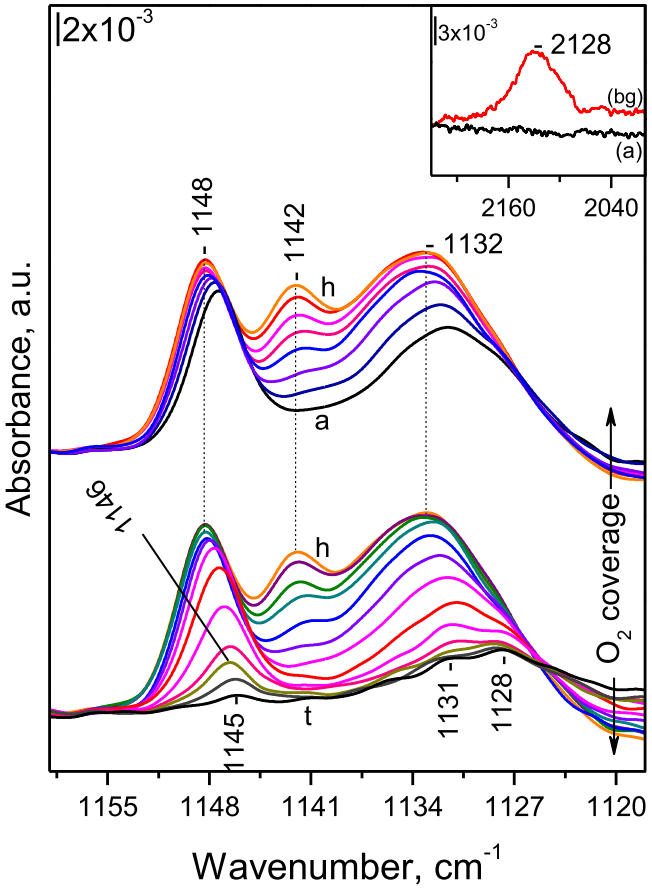

Fig. 3. FTIR spectra in the ν(O—O) stretching region of O_2 adsorbed at 100 K on reduced Pt/Ce-Zr/Al sample corresponding to the adsorbed oxygen species formed after each small dose of O_2 (~4.8×10^{-3} μmol doses up to a total pressure of 3.75 Torr O_2), (spectra *a–h*) and evolution of the spectra under successive evacuation (spectra *h–t*) gradually decreasing the surface oxygen coverage. The spectra are background corrected. The inset of the figure shows the background spectrum (*bg*) of the pre-reduced sample before O_2 adsorption and the one after the first small dose of O_2 (spectrum *a*).

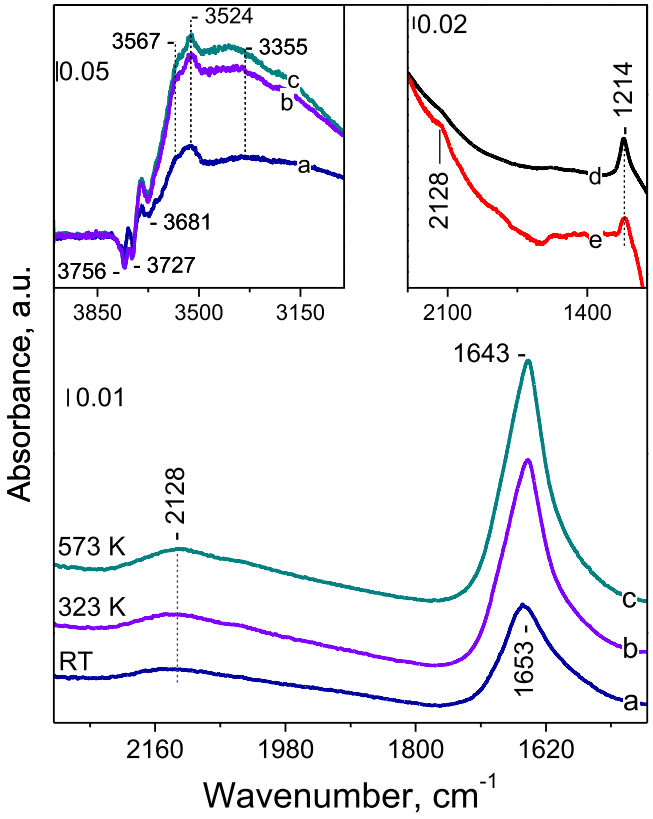

Fig. 4. FTIR spectra registered after interaction of activated Pt/Ce-Zr/Al sample with H_2 (75 Torr H_2 equilibrium pressure) at RT (a) and evolution of the spectra after each step of increasing the temperature in the range of 298–573 K (b, c). The insets of the figure show the spectral changes in the ν(OH) stretching region (on left) and the spectra of D_2 adsorbed at RT and 323 K (on right, spectra d and e). The spectra are background corrected.

surface mobility of oxygen *via* spill-over of oxygen/superoxide from metal sites to the support surface. The stretching mode of adsorbed O_2^- on metals [50,51] have been typical observed within 1110-1195 cm^{-1} and 1075- 1122 cm^{-1}. Thus, the presence of the bands at 1148 and 1142 cm^{-1} observed in our work at low-temperatures (Fig. 3) and also the features detected at 1144 and 1139 cm^{-1} at ambient temperatures, (Fig. S1, "Supplementary materials") can be assigned to the presence oxygen adsorbed species in the vicinity of noble metal centres.

On the basis of these observations, it can be suggested that the ability of the Pt/Ce-Zr/Al mixed oxide system to activate oxygen most likely originates from its relatively high population of oxygen vacancies located on/near the surface. This suggestion is consistent with earlier literature reports [47–49]. In these reports, it was shown that relatively high OSC of $Ce_xZr_{(1-x)}O_2$ mixed oxides can be correlated to their higher oxygen vacancy concentration located near the surface. The OSC of the cerium-zirconium mixed oxides decorated with precious metal sites (*e.g.* Rh, Pt, Pd) was also found [52] to strongly depend on the nature of the interface between the metal and the support material. Also, it was reported that OSC varied in a non-liner fashion as a function of the noble metal dispersion. It was demonstrated [52] that increasing the average size of the fcc noble metal nanoparticles increases the relative extent of the (111) facets on these particles where oxygen can adsorb stronger. Hence, these sites can boost oxygen adsorption/uptake and facilitate oxygen spill-over to the support surface [53].

3.2.4. *Interaction of Pt/Ce-Zr/Al sample with H_2*

In these experiments, H_2 (75 Torr H_2 equilibrium pressure) was adsorbed at ambient temperature on the Pt/Ce-Zr/Al catalyst which was initially pre-activated at 673 K in air for 1 h, followed by evacuation at the same temperature. Then, after cooling to room temperature, H_2 was introduced into the IR cell and the sample was heated in the presence of H_2 up to 573 K. The evolution of the FTIR spectra after each step of increasing temperature in the range of 298–573 K is presented in Fig. 4. The inset of the figure shows the spectral changes in the ν(OH) stretching region (left inset) and the spectra of D_2 adsorbed at RT and 323 K (right inset, spectra d and e).

It is visible that immediately after introduction of H_2 to the system at room temperature (spectrum a) two main IR features appeared at 2128 and 1643 cm^{-1}. The broad feature at 2128 cm^{-1} is associated with the forbidden $^2F_{5/2} - {}^2F_{7/2}$ electronic transition of Ce^{3+} ions and its presence is indicative [37,54,55] of oxygen vacancy formation. The band at 1643 cm^{-1} is attributed to the bending mode (δ_{H-O-H}) of molecular adsorbed water [54]. These two processes can be summarized in reactions (*4, 5*) and (6):

$$H_2(g) \rightarrow 2H(ads) \quad (4)$$

$$Ce^{4+}(surf) + O^{2-}(surf) + H(ads) \rightarrow Ce^{3+}(surf) + OH^-(ads) + *(vacancy) \quad (5)$$

$$Ce^{4+}(surf) + OH^-(ads) + H(ads) \rightarrow Ce^{3+}(surf) + H_2O(ads) + *(vacancy) \quad (6)$$

Similar to the H_2 adsorption experiments, D_2 adsorption carried out at RT and 323 K (spectra *d* and *e* in the inset on right, respectively) also

clearly showed the appearance of two features at 2128 (shoulder) and 1214 cm^{-1}. The band at 1214 cm^{-1} was assigned to the bending mode (δ_{D-O-D}) of adsorbed molecular D_2O. No significant changes can be seen with a further increase of the reduction temperature up to 573 K (Fig. 4). The simultaneous appearance of both features immediately after H_2 (or D_2) exposure at RT clearly indicates that the reduction of ceria can easily be triggered in the presence of H_2 even at ambient temperature. This process is probably assisted by the Pt sites which are well-known [56] to dissociate adsorbed hydrogen. This argument is also in good agreement with various former reports [54,55,57], where (Pt, Pd, Au)/$Ce_xZr_{1-x}O_2$ systems were found to facilitate H_2/(D_2) dissociation. Atomic hydrogen or deuterium species adsorbed on the noble metal sites can easily migrate to the support surface and promote ceria reduction *via* creation of oxygen vacancies.

The analysis of the FTIR spectra in the ν(OH) stretching region (inset on the left of Fig. 4) revealed that immediately after H_2 exposure at RT, three negative bands at 3756, 3727 and 3681 cm^{-1} appeared along with the development of multiple overlapping positive IR features at 3524, ~ 3587 cm^{-1} (shoulder) and a very broad feature at around 3355 cm^{-1}. Appearance of these features suggests the formation of H-boned hydroxyl groups (more details are provided in the next section).

3.2.5. D_2 adsorption

In order to elucidate the complex overlapping OH signals obtained after H_2 adsorption, we performed complementary D_2 adsorption experiments on Pt/Ce-Zr/Al, which allowed us to switch to the O—D stretching region of the IR spectrum providing higher signal to noise ratio as well as revealing additional information for vibrational peak assignments. In these experiments, precisely controlled and small doses of D_2 equivalent to ~ 9.5×10^{-2} μmol were successively introduced onto the activated sample surface at ambient temperature (298 K) until an equilibrium pressure of 75 Torr D_2 was reached in the IR cell. Then, the sample was heated to higher temperatures within 323–673 K. The spectra (*a–e*) in Fig. 5 were obtained after stepwise increase of the of D_2 equilibrium pressure at RT up to 75 Torr (spectrum *f*). Next, in the presence of 75 Torr D_2, temperature was gradually increased within 298–673 K with 50 K steps (spectra *f-n*). The insets of Fig. 5show the spectral changes in the ν(O—H) stretching region (left) and δ_{D-O-D} bending region (right).

As can be seen in the left inset of Fig. 5, the original ν(O—H) stretching bands corresponding to isolated O—H groups of Pt/Ce-Zr/Al (3753, 3727, and 3681 cm^{-1}) quickly disappear in presence of D_2(three negative features located in the ν(O—H) stretching region),*i.e.* their protons are exchanged with D^+. Indeed, this process is accompanied by concomitant appearance of three positive bands indicative of O—D modes with maxima at 2757, 2722 and 2714 cm^{-1} and a broad feature at around 2500 cm^{-1} (Fig. 5 spectra *a–f*). The broad band at ~2500 cm^{-1} characterizes deuteroxyls revealing intermolecular hydrogen-bonding interactions. This clearly implies that D_2 adsorption occurs by dissociation and gradual replacement of protium ions with deuterium ($OH + D \rightarrow OD + H$) in the surface hydroxyl groups. Comparison of the intensities of the respective bands indicates almost complete (*i.e.* 100%) deuteroxylation. The experimentally obtained ratio of the hydroxyl and deuteroxyl vibrational frequencies is 1.36, which is in very good agreement with the theoretical value of 1.37 [34].

In addition to the deuteration of the surface hydroxyl groups, the gradual increase of the D_2 pressure also leads to the development of two additional positive IR features at 2613 and 2642 cm^{-1} (shoulder). This process is also accompanied by the formation of small quantities of molecularly adsorbed D_2O which is evident by the appearance of a band at 1212 cm^{-1} immediately after the first few doses of D_2 at RT (right inset of Fig. 5, spectrum e). This implies that the reduction of ceria can easily be triggered, and the oxygen vacancies can be produced immediately when D_2 exposure is initiated. The band at 2128 cm^{-1} associated with the forbidden $^2F_{5/2} - {}^2F_{7/2}$ electronic transition of Ce^{3+} ions becomes more discernible after D_2 evacuation/desorption, as shown in Fig. 6B.

The results from these experiments suggest that D_2 adsorption may occur through heterolytic dissociation and reduction of ceria, leading to the formation of adsorbed molecular water. Further, water molecules produced upon ceria reduction may interact with the O—D groups through H-bonding and this could cause the appearance of wider and more intense bands shifted to lower wavenumbers compared. Thus, the bands observed in the spectra at 2638 and 2606 cm^{-1} in Fig. 5 were assigned to H–bonded deuteroxyls (including the O—D groups interacting with the water and the O—D groups of D_2O).

In order to investigate the thermal stability of the O—D groups revealing intermolecular hydrogen bonding interactions, Pt/Ce-Zr/Al sample was first exposed to 75 Torr D_2 equilibrium pressure at RT and then the sample was evacuated. Next, temperature was gradually increased within 298–673 K in vacuum (Fig. 6). Fig. 6A shows the corresponding O—D stretching region, while Fig. 6B presents the spectral region associated with the forbidden $^2F_{5/2} - {}^2F_{7/2}$ electronic transition of Ce^{3+} ions.

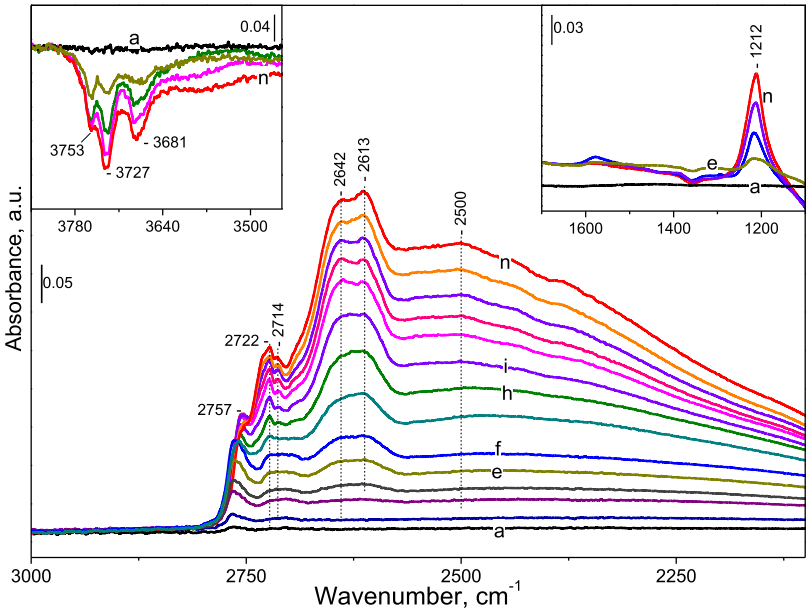

Fig. 5. FTIR spectra for D_2 adsorption on Pt/Ce-Zr/Al: (a–f) after each small dose of D_2 (~ 9.5×10^{-2} μmol/dose up to a total D_2 equilibrium pressure of 75 Torr) in the IR cell. (f–n) Stepwise increase in temperature within 298–673 K in the presence of 75 Torr D_2. The insets of the figure show the spectral changes in the ν(O—H) stretching region (left) and in the bending mode (δ_{D-O-D}) region of molecularly adsorbed D_2O (right). The spectra are background corrected.

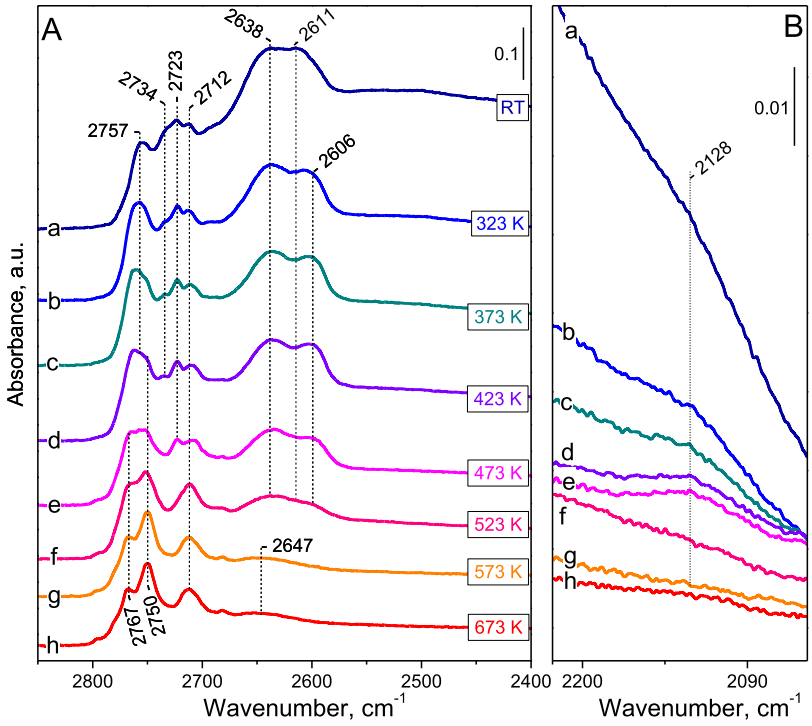

Fig. 6. FTIR spectra obtained after saturation of Pt/Ce-Zr/Al with 75 Torr D_2 at RT followed by evacuation at RT (spectrum a) and successive heating in vacuum at the given temperatures (spectra b–h). (A) O—D stretching region, (B) spectral region for the forbidden $^2F_{5/2} - {}^2F_{7/2}$ electronic transition of Ce^{3+} ions. The spectra are background corrected.

It can be seen in Fig. 6A that O—D groups revealing intermolecular hydrogen bonding interactions on Pt/Ce-Zr/Al (*i.e.* broad vibrational features at *ca.* 2650-2610 cm^{-1}) are relatively less stable and gradually vanish from the surface with increasing temperatures, leaving behind only isolated O—D groups characterized by the sharp features within 2700-2800 cm^{-1}. Fig. 6B indicates that during the loss of the O—D groups revealing intermolecular hydrogen bonding interactions on Pt/Ce-Zr/Al as a result of vacuum annealing at higher temperatures within 523–673 K, reduced Ce^{3+} sites are re-oxidized to Ce^{4+} probably by the thermally activated adsorbed D_2O and OD species which can readily diffuse on the surface [37] and fill the oxygen vacancies, followed by an electron transfer from Ce^{3+} sites.

3.2.6. *NO + O_2 adsorption at ambient temperature*

In attempt to understand if the O—D groups revealing intermolecular hydrogen bonding interactions which were generated upon ceria reduction in the presence of D_2, also participated in the NO_x adsorption process and thus contributed towards NO_x reactivity of the Pt/Ce-Zr/Al catalyst, NO_x adsorption over the sample pre-exchanged with deuterium was carried out at ambient temperature.

First, the Pt/Ce-Zr/Al catalyst which was initially treated with 75 Torr D_2 at 673 K for 15 min. This is followed by cooling of the system to ambient temperature and evacuation (see the bottom inset in Fig. 7B (background spectrum *bg1*). Then NO (*ca.* 3.75 Torr equilibrium pressure) was introduced into the IR cell. As a next step, small doses of O_2 were successively added to the system to increase oxygen partial pressure up to 6 Torr (Fig. 7, spectra *a–g)*. For comparison, the top inset in Fig. 7A and B shows the N–O and O—H stretching regions of the non-deuteroxylated Pt/Ce-Zr/Al sample before (background spectrum *bg2*) and after NO + O_2 adsorption (spectra *g2*). Note that the sample is dehydrated.

Adsorption of NO hardly affects the background spectrum bg1 of the sample. Successive introduction of small doses of O_2 (Fig. 7A, spectra a–f) leads to the appearance of several bands at 1623, 1586, 1569, 1494, 1430, 1309, 1267 (shoulder), 1229, 1205, 1040 (shoulder) and 1013 cm^{-1}. All of these features continuously grow and reach their maximum intensities with increasing oxygen pressure (spectrum g) with the exception of the feature at 1205 cm^{-1} which is significantly suppressed.

Comparative analysis of the IR spectra depicted in Fig. 7A, with that of the NO_x features observed in one of our former reports focusing on NO + O_2 adsorption on Pt/Ce-Zr/Al without a preliminary D_2 introduction allows elucidation of the features given in Fig. 7B. In the light of this previous work [29] it can be suggested that initial small doses of O_2 onto the NO-Pt/Ce-Zr/Al system results in the formation of surface nitro/nitrito (-NO_2/-ONO) species. The characteristic bands identifying the presence of these compounds appear in the ν(N–O) spectral region at 1229 and 1205 cm^{-1}. They were assigned to originate from the ν_{as} of bridging nitrites. The band at 1040 cm^{-1} corresponds to the ν(N—O) modes of non-symmetric nitrites bound more strongly to the surface *via* one of the oxygen atoms. Increasing the amount of O_2 induces the oxidation of nitrites to nitrates [29,34,58,59] and the intensities of the nitrate-related IR bands (*i.e.* bridged/bidentate nitrates) increase at the expense of the nitrite features. The band at 1309 cm^{-1} along with the feature at 1013 cm^{-1} can be attributed to symmetrical nitrates which are characteristic in the presence of some water.

NO + O_2 adsorption over Pt/Ce-Zr/Al surface pre-exchanged with deuterium is accompanied by the appearance of several additional adsorption features which were not detected when initial D_2 adsorption step was not performed (see spectrum g2 in the inset of Fig. 7A). These bands are visible in the spectra in Fig. 7A located at ~1494 and 1430 cm^{-1}. We assign these features to the nitrato (-ONO_2) complexes coordinated to the deuteroxyls. This suggestion was further supported by the analysis of the spectra shown in Fig. 7B where the process of NO_x adsorption is accompanied by the appearance of several negative features located in the ν(O—D) stretching region. The appearance of the negative features at 2757 and 2723 cm^{-1} reveals that the NO + O_2 adsorption takes place concomitant to the consumption of the isolated O—D groups. The bands at ~2638 and 2611 cm^{-1} formed after the interaction of the Pt/Ce-Zr/Al system with deuterium (see the background spectrum *bg1* presented in bottom inset of Fig. 7B) also gradually attenuate and appear as negative features forming dips in the spectral line shape (Fig. 7B, spectra *a-g*). These observations demonstrate the interaction of surface hydroxyls with NO_x species.

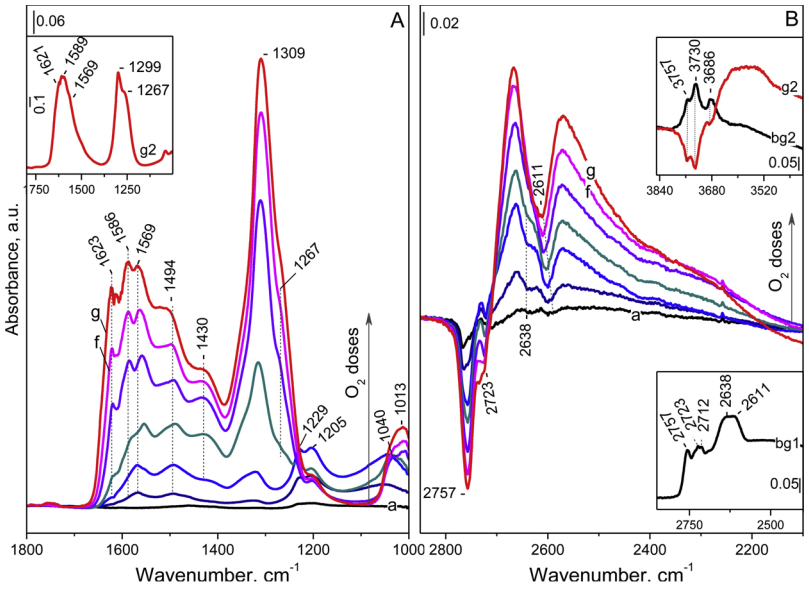

Fig. 7. FTIR spectra in the ν(N—O) (panel A) and ν(O—D) (panel B) stretching regions of NO + O_2 co-adsorbed (3.75 Torr NO and 6 Torr O_2 equilibrium pressure) at RT on the pre-exchanged with deuterium Pt/Ce-Zr/Al catalyst. Evolution of the spectra during gradual adsorption of small doses of O_2 (spectra *a–f*) and NO + O_2 co-adsorbed on the sample surface at NO + O_2 equilibrium pressure (spectrum *g*). All spectra are background and NO gas-phase corrected. The inset of Fig. 7B at the bottom shows the background spectrum of the sample pre-exchanged with deuterium (spectrum *bg1*). The inset on the top shows the background spectrum of the non-deuterated sample and the NO + O_2 co-adsorption the non-deuterated sample (spectra *bg2* and *g2, respectively*).

3.2.7. NO_x – TPD

To investigate the thermal stability of the adsorbed NO_x species, we have also carried out TPD experiments on the Pt/Ce-Zr/Al sample containing pre-adsorbed NO_x, as described in the experimental section. In order to see the effect of the interaction of the Pt/Ce-Zr/Al system with H_2, which could significantly increase the reactivity by enriching the surface with H-bonded OH groups, the pre-treatment step prior to the NO_x adsorption was performed in two different manners. In the first experiment (i), the Pt/Ce-Zr/Al sample was pre-reduced with H_2 (75 Torr H_2 equilibrium pressure) at 673 K and then evacuated at 423 K. In the second one (ii), the sample was pre-reduced with H_2 at 673 K, then evacuated at 673 K. Thus, it was possible to follow the changes in the NO_x-TPD profiles of the Pt/Ce-Zr/Al sample which was enriched (*i*) or depleted (*ii*) in H-bonded OH groups.

Evolution of the total NO_x ($NO + NO_2$) release as a function of temperature during the NO_x-TPD, in experiments (i) and (ii) is presented in Fig. 8A. N_2O and O_2 desorption profiles for these experiments are also shown in Fig. 8B and C, respectively. NO_x-TPD curves can be deconvoluted into four peaks (as presented in Fig. 8A) using a Gaussian curve-fitting method. Obtained areas under the fitted peaks were used to compare different NO_x adsorption contributions associated with different phases/domains of the ternary oxide Pt/Ce-Zr/Al system without any quantitative analysis and kinetics justification.

TPD profiles corresponding to the Pt/Ce-Zr/Al system pre-treated with H_2 in both cases (Fig. 8, *i and ii*) showed very similar NO_x desorption features. However, in contrast to the sample where H_2 was evacuated at 673 K, total NO_x release from the sample evacuated at 423 K was greater in amount. In addition, it can be also seen in Fig. 8B and 8C that NO_x decomposition is also accompanied by the production of small quantities of N_2O and O_2. N_2O and O_2 desorption channels are much more pronounced for the sample enriched with H-bonded OH groups.

NO_x – TPD of Pt supported on CeO_2/γ-Al_2O_3, ZrO_2/γ-Al_2O_3 and CeO_2-ZrO_2/γ-Al_2O_3 have been thoroughly discussed in our previous work [29]. These former results showed that the Pt/Ce-Zr/Al system is characterized by the presence of at least two different types of NO_x species adsorbed on ceria and another NO_x species adsorbed on zirconia with distinctively different thermal stabilities.

In agreement with this former report [29] and other studies in the literature [60–64], the low–temperature TPD signal at ~ 390 K in Fig. 8A can be assigned to the thermal decomposition of the weakly NO_x adsorbed species, formed mostly on the Al^{3+} adsorption sites. The second NO_x desorption feature at ~ 507 K can be tentatively assigned

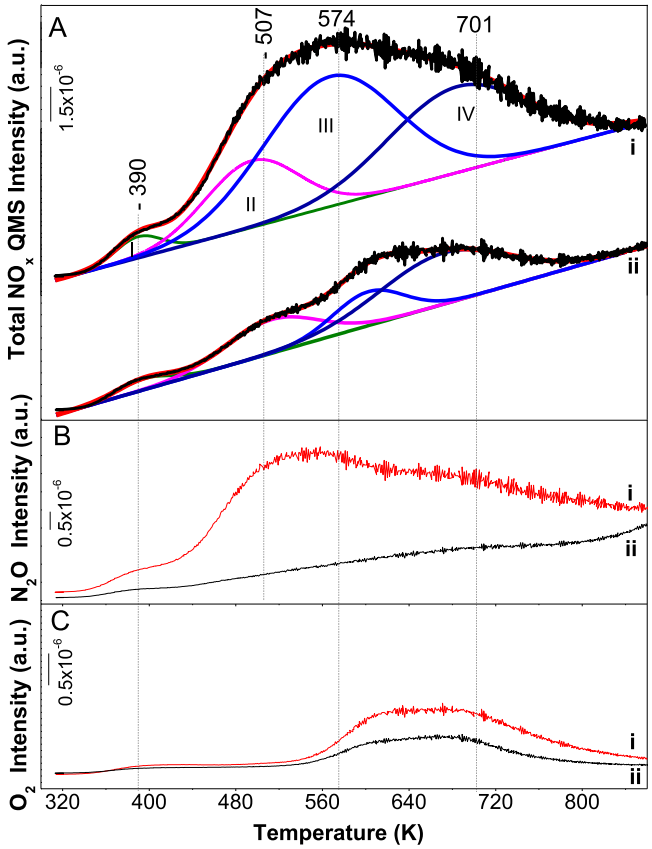

Fig. 8. Evolution of the total NO_x ($NO + NO_2 + N_2O + N_2$) release as function of temperature during TPD (panel A) over the Pt/Ce-Zr/Al pre-reduced in H_2 at 673 K and then evacuated at 423 K (i) or 673 K (ii). Panels (B) and (C) show the N_2O and O_2 concentration profiles for these experiments, respectively.

to desorption of the more stable nitrates bound to surface CeO_2 species strongly interacting with the Pt. The desorption feature at *ca.* 574 K is attributed to the decomposition of the NO_x species strongly bonded to bulk CeO_2, while the shoulder at ~ 701 K is likely due to desorption of more stable NO_x ad-species on zirconia.

On the basis of these observations, it can be concluded that the pre-treatment with hydrogen and enrichment of the surface with H-bonded

hydroxyl can significantly increase the NO oxidation and NO_x storage. The finding can be interesting for passive NO_x adsorbers (PNA) [65] that operate at room temperature.

4. Conclusions

The main conclusions of the presented results can be summarized as follows:

(a) Detailed information regarding the nature of metallic Pt sites and various types of surface acid and oxygen-deficient adsorption sites on the sample Pt/Ce-Zr/Al surface pre-reduced with hydrogen at 723 K was obtained by low–temperature CO or O_2 adsorption, monitored *via in-situ* FTIR. The results revealed that reduced Pt/Ce-Zr/Al system is characterized by the presence of oxygen vacancies located in close vicinity of Ce^{3+} centres and metallic Pt that exists on the surface with different particle sizes. Adsorption of molecular oxygen on the vacancies occurred by electron donation from the neighbouring Ce^{3+} species, leading to the formation of superoxide (O_2^-) adspecies and oxidation of Ce^{3+} to Ce^{4+} ions. The ability of the reduced Pt/Ce-Zr/Al surface to activate oxygen was found to originate most likely from its relatively high population of oxygen vacancies located on/near the surface.

(b) The analysis of the FTIR spectra upon interaction of Pt/Ce-Zr/Al mixed oxide system with H_2 or D_2 clearly revealed that adsorption occurs easily through heterolytic dissociation at ambient temperature. D_2 adsorption occurs by dissociation and gradually replacement of protium ions with deuterium (*D→H exchange*) in the isolated O−H groups (deuteroxylation degree *ca.* 100%). The process is accompanied by the reduction of Ce^{4+} to Ce^{3+} ions, leading to the formation of molecularly adsorbed water. It was found that the reduction of ceria can easily be triggered at ambient temperature in the presence of H_2/D_2. Water produced upon reduction may interact with the isolated hydroxyls/deuteroxyls groups through H-bonding and this could facilitate the formation of O−H/O-D groups with intermolecular hydrogen bonding interactions. These later species are relatively stable and gradually vanish with increasing temperatures above 523 K, leaving behind only isolated hydroxyls.

(c) The Pt/Ce-Zr/Al sample pre-treated in a way to achieve a surface enriched or depleted with intermolecularly hydrogen-bonded hydroxyls/deuteroxyls was analysed through NO_x adsorption/desorption experiments. The surface enriched with H-bonded hydroxyls is characterized by an enhanced NO_x storage ability. Thus, it was concluded that presence of H-bonded hydroxyls could play a significant role in the NO_x adsorption mechanism.

Acknowledgments

The authors gratefully acknowledge the financial support by the Bulgarian National Science Fund (project No: DN 19/2). EO acknowledges the scientific collaboration with TARLA project founded by the Ministry of Development of Turkey (project code: DPT2006K-120470). Authors acknowledge SASOL GmbH for providing Puralox alumina support materials.

Appendix A. Supplementary data

Supplementary material related to this article can be found, in the online version, at doi:https://doi.org/10.1016/j.cattod.2019.02.056.

References

[1] H.L. Fang, H.F.M. DaCosta, Appl. Catal. B: Environ. 46 (2003) 17–34.
[2] S. Matsumoto, Y. Ikeda, H. Suzuki, M. Ogai, N. Miyoshi, Appl. Catal. B: Environ. 25 (2000) 115–124.
[3] K. Yamazaki, T. Suzuki, N. Takahashi, K. Yokota, M. Sugiura, Appl. Catal. B: Environ. 30 (2001) 459–468.
[4] H. Hirata, I. Hachisuka, Y. Ikeda, S. Tsuji, S. Matsumoto, Top. Catal. 16/17 (2001) 145–149.
[5] R. Burch, Catal. Rev. − Sci. Eng. 46 (2004) 271–334.
[6] G. Liu, P.-X. Gao, Catal. Sci. Technol. 1 (2011) 552–568.
[7] S. Roy, A. Baiker, Chem. Rev. 109 (2009) 4054–4091.
[8] C. Bormann, N. Rodríguez, P. Araya, S. Guerrero, Catal. Commun. 76 (2016) 76–81.
[9] C. Tang, H. Zhang, L. Dong, Catal. Sci. Technol. 6 (2016) 1248–1364.
[10] D. Mukherjee, B.M. Reddy, Catal. Today 60 (2017) 1673–1681.
[11] M.V. Ganduglia-Pirovano, A. Hofmann, J. Sauer, Surf. Sci. Rep. 62 (2007) 219–270.
[12] A. Trovarelli, Catal. Rev. Sci. Eng. 38 (1996) 439–520.
[13] J. Kašpar, P. Fornasiero, M. Graziani, Catal. Today 50 (1999) 285–298.
[14] Z. Say, E.I. Vovk, V.I. Bukhtiyarov, E. Ozensoy, Appl. Catal. B: Environ. 1420143 (2013) 89–100.
[15] M.A. Peralta, V.G. Milt, L.M. Cornaglia, C.A. Querini, J. Catal. 242 (2006) 118–130.
[16] J.H. Kwak, D.H. Kim, J. Szanyi, C.H.F. Peden, Appl. Catal. B: Environ. 84 (2008) 545–551.
[17] N.V. Skorodumova, S.I. Simak, B.I. Lundqvist, I. Abrikosov, B. Johansson, Phys. Rev. Lett. 89 (2002) 166601.
[18] J. Yu, Z. Si, L. Chen, X. Wu, D. Weng, Appl. Catal. B: Environ. 163 (2015) 223–232.
[19] N.Le. Phuc, E.C. Corbos, X. Courtois, F. Can, P. Marecot, D. Duprez, Appl. Catal. B: Environ. 93 (2009) 12–21.
[20] T. Vinodkumar, B.G. Rao, B.M. Reddy, Catal. Today 263 (2015) 57–64.
[21] C. Shi, Y. Ji, U.M. Graham, G. Jacobs, M. Crocker, Z. Zhang, Y. Wang, T.J. Toops, Appl. Catal. B: Environ. 119-120 (2012) 183–196.
[22] L.F. Liotta, A. Longo, A. Macaluso, A. Martorana, G. Pantaleo, A.M. Venezia, G. Deganello, Appl. Catal. B: Environ. 48 (2004) 133–149.
[23] L.F. Liotta, A. Macaluso, A. Longo, G. Pantaleo, A. Martorana, G. Deganello, Appl. Catal. A: Gen. 240 (2003) 295–307.
[24] B.M. Reddy, T. Vinodkumar, D.N. Durgasri, A. Rangaswamy, Proc. Natl. Acad. Sci. India, Sect. A: Phys. Sci. 87 (2017) 155–161.
[25] R. Di Monte, P. Fornasiero, S. Desinan, J. Kaspar, J.M. Gatica, J.J. Calvino, E. Fonda, Chem. Mater. 16 (2004) 4273–4285.
[26] R. Di Monte, J. Kašpar, Catal. Today 100 (2005) 27–35.
[27] M. Haneda, T. Morita, Y. Nagao, Y. Kintaichi, H. Hamada, Phys. Chem. Chem. Phys. 3 (2001) 4696–4700.
[28] J.R. Theis, Catal. Today 267 (2016) 93–109.
[29] S. Andonova, Z.A. Ok, N. Drenchev, E. Ozensoy, K. Hadjiivanov, J. Phys. Chem. C 122 (2018) 12850–12863.
[30] G. Bergeret, P. Gallezot, Particle size and dispersion measurements, Handbook of Heterogeneous Catalysis Handbook of Heterogeneous Catalysis, (2008), pp. 439–442.
[31] NIST Chemistry WebBook, SRD 69; https://webbook.nist.gov/chemistry/.
[32] V. Azároff, Elements of X-ray Crystallography, McGraw-Hill, NewYork, 1968 p. 254.
[33] G. Busca, Adv. Catal. 57 (2014) 319–404.
[34] K. Hadjiivanov, Adv. Catal. 57 (2014) 99–318.
[35] M.Y. Mihaylov, E.Z. Ivanova, H.A. Aleksandrov, P.St. Petkov, G.N. Vayssilov, K.I. Hadjiivanov, Appl. Catal., B: Environ. 176-177 (2015) 107–119.
[36] C. Binet, M. Daturi, J.-C. Lavalley, Catal. Today 50 (1999) 207–225.
[37] S.M. Schimming, G.S. Foo, O.D. LaMont, A.K. Rogers, M.M. Yung, A.D. D'Amico, C. Sievers, J. Catal. 329 (2015) 335–347.
[38] N. Drenchev, I. Spassova, E. Ivanova, M. Khristova, K. Hadjiivanov, Appl. Catal. B: Environ. 138-139 (2013) 362–372.
[39] H.A. Aleksandrov, K.M. Neyman, K.I. Hadjiivanov, G.N. Vayssilov, Phys. Chem. Chem. Phys. 18 (2016) 22108–22121.
[40] P. Bazin, O. Saur, J.C. Lavalley, M. Daturi, G. Blanchard, Phys. Chem. Chem. Phys. 7 (2005) 187–194.
[41] J. Happel, V. Mysliveček, F. Johánek, O. Dvořák, Y. Stetsovych, Y. Lykhach, V. Matolín, J. Libuda, J. Catal. 289 (2012) 118–126.
[42] G. Rupprechter, T. Dellwig, H. Unterhalt, H.-J. Freund, J. Phys. Chem. B 105 (2001) 3797–3802.
[43] K. Chakarova, M. Mihaylov, K. Hadjiivanov, Microporous Mesoporous Mater. 81 (2005) 305–312.
[44] C. Li, K. Domen, K.-ichi Maruya, T. Onishi, J. Am. Chem. Soc. 11 (1989) 7683–7687.
[45] Y.M. Choi, H. Abernathy, H.-T. Chen, M.C. Lin, M. Liu, Chem. Phys. Chem. 7 (2006) 1957–1963.
[46] C. Li, K. Domen, K.-ichi Maruya, T. Onishi, J. Catal. 123 (1990) 436–442.
[47] S. Bedrane, C. Descorme, D. Duprez, Stud. Surf. Sci. Catal. 138 (2001) 125.
[48] S. Bedrane, C. Descorme, D. Duprez, Catal. Today 75 (2002) 401–405.
[49] C. Descorme, Y. Madier, D. Duprez, J. Catal. 196 (2000) 167.
[50] J. Schmidt, Ch. Stuhlmann, H. Ibach, Surf. Sci. 284 (1993) 121–128.
[51] M. Shao, P. Liu, R.R. Adzic, J. Am. Chem. Soc. 128 (2006) 7408–7409.
[52] C. Descorme, Y. Madier, D. Duprez, T. Birchem, Stud. Surf. Sci. Catal. 130 (2000) 347–352.
[53] C. Li, Y. Song, Y. Chen, Q. Xin, X. Han, W. Li, Can Li, Qin Xin (Eds.), Spillover and Migration of Surface Species on Catalysts, Elsevier Science B.V., 1997.
[54] S.E. Collins, J.M. Cíes, E. del Río, M. López-Haro, S. Trasobares, J.J. Calvino, J.M. Pintado, S. Bernal, J. Phys. Chem. C 111 (2007) 14371–14379.
[55] F.C. Gennari, T. Montini, N. Hickey, P. Fornasiero, M. Graziani, Appl. Surf. Sci. 252 (2006) 8456–8465.
[56] T. Gomez, E. Florez, J.A. Rodriguez, F. Illas, J. Phys. Chem. C 115 (2011) 11666–11672.
[57] F.C. Gennari, C. Neyertz, G. Meyer, T. Montini, P. Fornasiero, Phys. Chem. Chem. Phys. 8 (2006) 2385–2395.
[58] J. Szanyi, J.H. Kwak, R.J. Chimentao, C.H.F. Peden, J. Phys. Chem. C 111 (2007)

2661–2669.
[59] E. Ozensoy, D. Herling, J. Szanyi, Catal. Today 136 (2008) 46–54.
[60] J. Szanyi, J.H. Kwak, R.J. Chimentao, C.H.F. Peden, J. Phys. Chem. C 111 (2007) 2661–2669.
[61] S.M. Andonova, G.S. Şentürk, E. Ozensoy, J. Phys. Chem. C 114 (2010) 17003–17016.
[62] E. Kayhan, S. Andonova, G.S. Şentürk, Ch.C. Chusuei, E. Ozensoy, J. Phys. Chem. C 114 (2010) 357–369.
[63] S. Andonova, V. Marchionni, M. Borelli, R. Nedyalkova, L. Lietti, L. Olsson, Appl. Catal. B: Environ. 132-133 (2013) 266–281.
[64] Y. Ji, D. Xu, Sh. Bai, U. Graham, M. Crocker, B. Chen, Ch. Shi, D. Harris, D. Scapens, J. Darab, Ind. Eng. Chem. Res. 56 (2017) 111–125.
[65] Y. Gu, W.S. Epling, Appl. Catal. B 570 (2019) 1–14.